Acta Cryst B
STRUCTURAL SCIENCE
CRYSTAL ENGINEERING
MATERIALS

ISSN 2052-5206

Metastable disordered phase in flash-frozen Prussian Blue analogues

Yevheniia Kholina,[a] Janine Dössegger,[b] Mads C. Weber[c] and Arkadiy Simonov[a]*

[a]Department of Materials, ETH Zürich, 8093 Zürich, Switzerland, [b]Department of Physics, ETH Zürich, 8093 Zürich, Switzerland, and [c]Institut des Molécules et Matériaux du Mans, UMR 6283 CNRS, Le Mans Université, 72085 Le Mans, France. *Correspondence e-mail: arkadiy.simonov@mat.ethz.ch

Received 16 November 2021
Accepted 2 February 2022

Edited by M. Spackman, University of Western Australia, Australia

Keywords: diffuse scattering; Prussian blue analogues; metastable phase transition; IR spectroscopy.

Supporting information: this article has supporting information at journals.iucr.org/b

A new metastable phase in flash-frozen disordered Prussian blue analogues is reported. The phase is characterised by the appearance of diffuse scattering clouds and the reduction of the local structure symmetry: from cubic to a tetragonal or lower space group. The phase transition is characterised by the translational modulation of the structure and is likely caused by the freezing of the water confined in the pores of the structure.

1. Introduction

Prussian blue analogues, $M[M'(CN)_6]_{1-x}\cdot nH_2O$, which we abbreviate here as $M[M']$ (M and M' = transition metal ions), belong to a diverse family of cyanide materials, which are intensely investigated for their potential application for hydrogen storage (Kaye & Long, 2005), sensor applications (Karyakin, 2017), as catalysts (Peeters *et al.*, 2013) and electrode materials (Wessells *et al.*, 2011). They can also host a wealth of phenomena of fundamental interest, including multiferroicity (Kong *et al.*, 2019), magnetic pole inversion (Ohkoshi *et al.*, 1997) and spin crossover phenomena (Papanikolaou *et al.*, 2006).

Despite their deceptively simple average structure, the real structure of Prussian blue analogues (PBAs) proves to be more challenging due to the presence of a large number of vacancies on the $M'(CN)_6$ site. Recent analysis using single crystal diffuse scattering (Simonov *et al.*, 2020) has shown that the distribution of these vacancies is not random: the vacancies tend to avoid each other, but due to frustration the order is followed only locally. Moreover, the degree of order strongly depends on the nature of the transition metal ions, as well as the sample synthesis conditions.

In this paper we focus on structural behavior of PBAs at low temperatures. By tracing the evolution of diffuse scattering of the Mn[Co] member of the Prussian blue family we show that below 200 K the material goes through a displacive transition. The speed of cooling is important, as the flash frozen samples enter a metastable phase which reduces symmetry from high-temperature cubic to, at most, tetragonal.

The phase transition is marked by the appearance of diffuse scattering clouds around Bragg peaks, and since identical diffuse clouds were also observed in Cd[Co], Mn[Mn] and Mn[Fe] compounds (Simonov *et al.*, 2020), we assume that the observed phase transition is characteristic for all the defective members of the Prussian blue family.

PBAs are known to be a delicate class of materials, where the structure depends not only on the material composition (Escax *et al.*, 2001) but also on the synthesis conditions

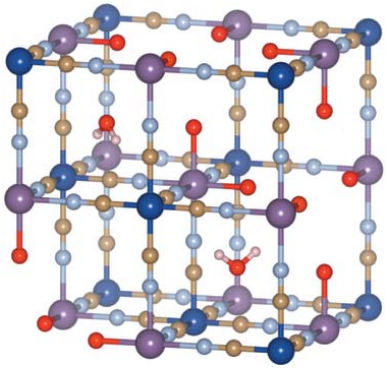

(Simonov *et al.*, 2020) and the dose of X-ray irradiation (Boström *et al.*, 2020). Our current work also shows that the temperature history can be equally important for determining the phase of these materials.

2. Methods and approaches

2.1. Synthesis

Single crystals of Mn[Co] PBAs were grown by the slow counter diffusion of aqueous solutions of divalent manganese(II) chloride, $MnCl_2$, and potassium hexacyanocobaltate(III), $K_3[Co(CN)_6]$, in Agar gel media. The growth was performed in 15 ml centrifuge tubes: first, the divalent Mn chloride (500 µmol) was dissolved in 1% Agar gel (10 ml) and poured into the centrifuge tube. After the gel was set, a water solution of potassium hexacyanometallate(III) (500 µmol in 5 ml H_2O) was added on top. The salts diffuse through the gel, resulting in precipitation of insoluble transparent cubic crystals with a length of 100–150 µm within one week. The precursor salts were used as supplied and without further purification. Agar and $K_3[Co(CN)_6]$ were purchased from Sigma-Aldrich, anhydrous $MnCl_2$ was purchased from Fluka.

2.2. Experimental details

Single-crystal diffraction experiments were carried out at the Swiss–Norwegian beamline (BM01) at the European Synchrotron Radiation Facility using an X-ray energy of 17.480 KeV ($\lambda = 0.7091$ Å) and at the Diamond Light Source using an X-ray energy of 17.998 KeV ($\lambda = 0.6889$ Å). Both beamlines are equipped with Pilatus 2M area photon-counting detectors. Samples were loaded on MiTeGen loops. The data were collected using a single 360° rotation scan around the φ axis with a 0.1° step per frame. The temperature was controlled using an Oxford Cryosystems Cryostream. Variable-temperature measurements were performed on a single Mn[Co] sample, which was first flash frozen to 90 K by quickly placing it in a cold gas stream. Afterwards, the crystal was slowly reheated to room temperature and then slowly cooled to 100 K. Diffuse scattering datasets were collected during heating and cooling cycles in 10 K steps.

Determination of the crystal orientation, indexing and integration of the Bragg peaks were performed using the software package *XDS* (Kabsch, 2010). The reconstruction was carried out using the *Meerkat* software (Simonov, 2019).

Disorder in Mn[Co] was analysed in direct space using the Three-Dimensional Difference Pair Distribution Function (3D-ΔPDF) approach (Weber & Simonov, 2012). 3D-ΔPDF is a Fourier transform of diffuse scattering and can be understood as the difference between the PDF of the real crystal structure and the Patterson function calculated from its average structure. Each signal in the 3D-ΔPDF at a position *uvw* corresponds to a pair of atoms *ij* in the structure such that $x_j - x_i = u$, $y_j - y_i = v$ and $z_j - z_i = w$. Signals in the 3D-ΔPDF can be positive or negative: for positive (negative) signals the interatomic pairs appear more (less) frequently in the real structure than in the average structure. For a more in-depth introduction see Weber & Simonov (2012). We have calculated 3D-ΔPDF using a custom script. In order to do it we have cleaned reconstructed diffuse scattering from Bragg peaks using the punch-and-fill procedure and also subtracted the spherically symmetric background.

Infrared light absorption spectra were recorded in the spectral range from 6000 to 400 cm^{-1} using a Fourier transform infrared spectrometer (Bruker Vertex 80v) in the temperature range from 300 K to 90 K using a Janis vacuum cryostat. The cooling was performed at a rate of 1 K min^{-1}, which is similar to the average rate during the slow cooling run in a diffraction experiment.

3. Results

3.1. Average structure and vacancy distribution of Prussian blue analogues

Prussian blue analogue Mn[Co] has a face-centered cubic average structure, with space group $Fm\bar{3}m$ and an average composition $Mn[Co(CN)_6]_{2/3}\cdot nH_2O$. Co and Mn atoms occupy the $1a$ $0,0,0$ and $1b$ $\frac{1}{2},\frac{1}{2},\frac{1}{2}$ sites in a simple NaCl-type arrangement and are connected by cyanide linkers, see Fig. 1. To maintain the charge balance between Mn^{2+} and $Co(CN)_6^{3-}$, one third of the $Co(CN)_6^{3-}$ units are replaced by vacancies. These vacancies are filled with structural (coordinated) and zeolitic (non-coordinated) water. The structural water is located at the $24e$ x, 0, 0 site, which completes the octahedral coordination of Mn^{2+} ions. The non-coordinated water is disordered in a large void and is usually modelled as two sites in the average structure: the high-symmetry site $8c$ $\frac{1}{4},\frac{1}{4},\frac{1}{4}$ in the middle of each unit-cell octant, surrounded by four positions at the $32f$ site x,x,x with $x \approx \frac{1}{6}$.

The $Co(CN)_6$ vacancies, although disordered on average, have a strong local order. In diffraction experiments, this local order manifests itself as characteristic squares of diffuse scattering around the Bragg peaks [Fig. 2(*a*)]. The detailed model explaining these signals is presented elsewhere (Simonov *et al.*, 2020).

3.2. Novel diffuse scattering in Mn[Co] on cooling

After the crystals of Mn[Co] are flash-frozen from room temperature to 90 K, new scattering features in the shape of diffuse clouds appear near Bragg peaks [Fig. 2(*b*)]. The speed

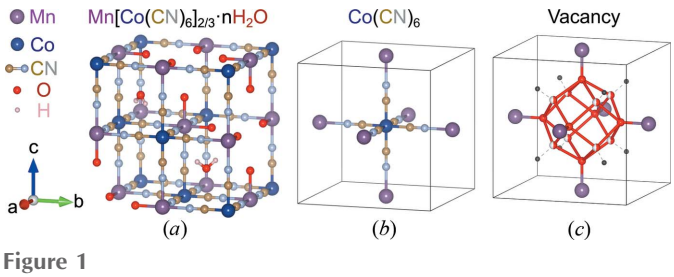

Figure 1
(*a*) Structure of $Mn[Co(CN)_6]_{2/3}$ PBA containing static disorder where one third of the $Co(CN)_6$ groups (*b*) are replaced by structural water and associated zeolitic water (*c*); black circles in (*c*) mark the center of water cavities located at the $[\frac{1}{4},\frac{1}{4},\frac{1}{4}]$ position.

of cooling is essential to obtain the clouds, as on slow cooling [Fig. 2(*c*)] they are almost absent. We identify three sets of clouds. The first is observed in the diffuse scattering sections with integer values of l at positions $h \pm \xi, k \pm \xi, l$, with $\xi \approx 0.38$, while the other two sets are found at the equivalent positions with the integer h and k indices.

The clouds break the room temperature cubic symmetry of the crystal, which is best seen in diffuse scattering from small samples. Fig. 3 presents the diffuse clouds around the Bragg reflection 666 from such a sample. The three sections 6*kl*, *h*6*l* and *hk*6 show different relative intensities, and thus the breaking of the cubic threefold rotation axis. The new phase has at most tetragonal symmetry, although the final symmetry may be even lower if the phase transition could be completed with fully developed diffraction satellites. Note that direct observation of such asymmetry requires small crystals, which increases the noise level in Fig. 3. Larger crystals tend to be perfect merohedral twins with equal volumes of crystallites in all possible orientations. As a result diffuse scattering from large crystals has an apparent cubic symmetry.

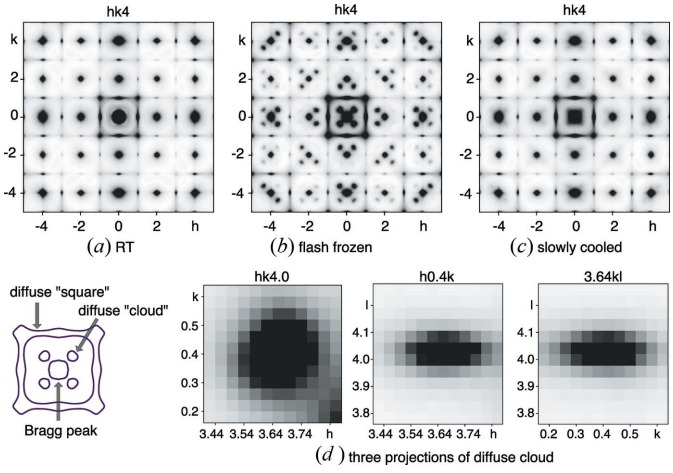

Figure 2
Single crystal diffraction layer *hk*4 from Mn[Co] at different temperatures: (*a*) at room-temperature diffraction shows only diffuse scattering from the vacancies, (*b*) after flash-cooling to 90K additional diffraction features in a shape of diffuse clouds appear; (*c*) samples which are slowly cooled to 100 K show only a weak hint of diffuse scattering clouds; (*d*) three cross sections of diffuse 'cloud' located at 1.64 0.38 4, near reflection 204. The cloud has the shape of a disc with a short dimension in the **c*** direction: HWHM of the cloud is 0.04 Å^{-1} in **a*** and **b*** directions, and 0.02 Å^{-1} in the **c*** direction corresponding to correlation lengths of 25 Å and 50 Å, respectively.

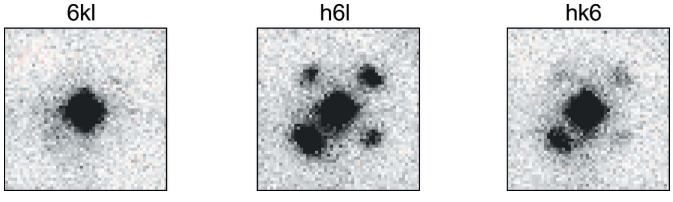

Figure 3
Diffuse scattering clouds around reflection 666 from a small single crystal of Mn[Co]. The clouds in the three sections 6*kl*, *h*6*l* and *hk*6 have different intensities and thus break the cubic symmetry which is present in the sample at room temperature.

To shed light on the structural origin of the diffuse clouds, we turn to the intensity distribution in reciprocal space. As we see from Fig. 4, the diffuse clouds of the first set increase in intensity in the *hkL* planes with increasing values of L, which indicates that the diffuse clouds are caused by a displacive distortion of the structure. The absence of diffuse intensity in the *hk*0 plane is systematic. By the projection-slice theorem (Neder & Proffen, 2008), such an absence can be observed only if the projection of the structure on the *ab* plane is not distorted. As we show below in §3.6 in this system systematic absences are caused by the fact that the distortions contain atomic displacements along the **c** direction only.

In a heating run starting at 90 K, the diffuse clouds gradually weaken and disappear at around 200 K (Fig. 5). At the same time the shape of the diffuse scattering from the vacancies also changes slightly (see region marked by a white arrow in Fig. 5).

Overall, we have identified a phase transition away from the cubic high-symmetry phase of Mn[Co]. This transition is driven by displacive distortions along the **c** direction. The new phase can only be reached by a fast cooling process, yet not under a slow sample cooling. This corroborates that the new phase causing the diffuse scattering clouds is metastable.

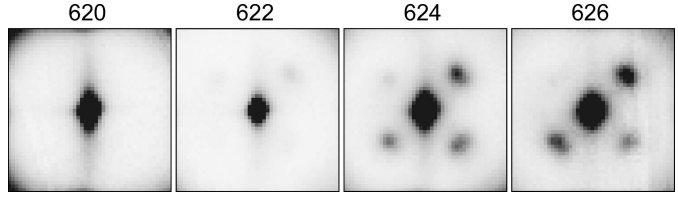

Figure 4
Diffuse scattering clouds in a flash-cooled sample around reflections 62L with $L = 2n$. The clouds are absent in the *hk*0 plane and become progressively stronger for larger values of L, which is representative for diffuse scattering of other *hkl* indices.

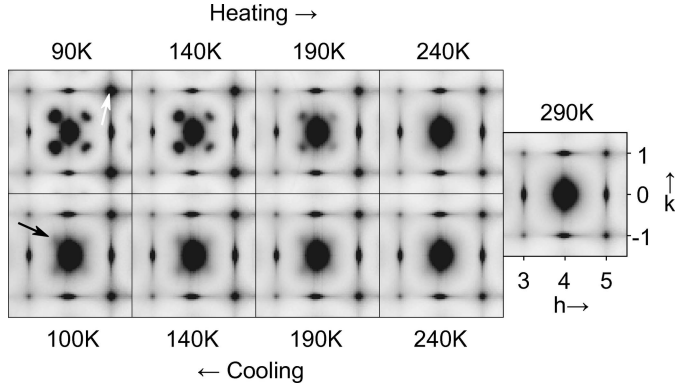

Figure 5
Evolution of diffuse scattering around reflection 404 during heating (top row) and cooling (bottom row). In addition to the disappearance of diffuse clouds, notice the variation in intensity of the diffuse scattering cloud near the position *hkl* = 514 (white arrow) and the appearance of a weak hint of diffuse clouds near the Bragg peaks on cooling (black arrow). The figure presents selected temperature points of the diffuse datasets which were collected at every 10 K.

3.3. Singular value decomposition analysis and the evolution of the order parameters

To quantitatively investigate the evolution of the structure with temperature, we have performed the singular value decomposition (SVD) analysis on the diffuse scattering dataset. The dataset comprises 40 three-dimensional diffuse scattering patterns for each temperature point, starting from quenched sample then heating to room temperature and finally followed by a slow cooling of the sample. SVD is a statistically robust method for extracting weak data variations in the presence of noise in the full three-dimensional volume of the data. In the present case, SVD reveals that the changes in the diffuse scattering dataset are satisfactorily explained by two components, and further exponents represent noise and experimental artifacts:

$$I_{\text{diffuse}}(T) \approx I_{\text{av}} + s_1(T)dI_1 + s_2(T)dI_2,$$

where I_{diffuse} is the diffuse scattering intensity, T is the sample temperature, I_{av} is the average of all 40 datasets, $s_i(T)$ are the temperature-dependent scale coefficients of the significant components and dI_i are the patterns of variation of diffuse scattering corresponding to each significant component. The evolution of s_1 and s_2 with temperature is presented on Fig. 6.

Component 1 is responsible for the appearance of the diffuse scattering clouds (see Fig. S2 in supporting information). It thus tracks the amplitude of the displacive distortion of the structure. In addition, component 1 also represents the changes of the diffuse squares, indicating slight variations of the structure factor of vacancies with temperature. At room temperature the clouds are absent which is achieved with the numerical value of $s_1 \sim -0.4$, as at this stage $s_1(T)dI_1$ compensates for the clouds observed in I_{av} (Fig. S2 in supporting information).

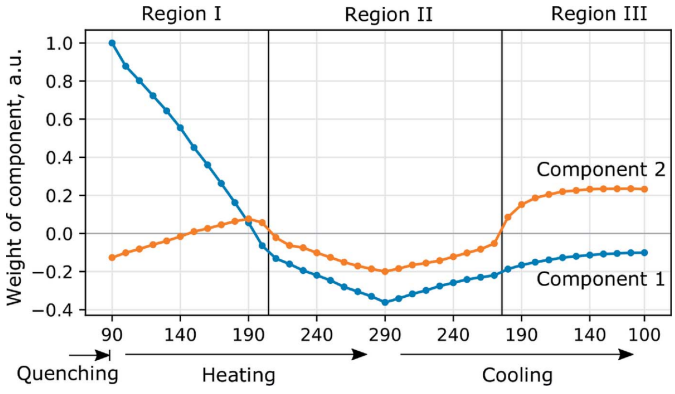

Figure 6
Temperature evolution of the significant components 1 and 2 of the singular value decomposition that track the changes in the diffuse diffraction data with temperature in a heating run after quenching the sample, followed by a slow cooling. The components are scaled according to their singular values. Component 1 mostly follows the intensity of the diffuse clouds and is at its minimum when the clouds are essentially absent at room temperature; component 2 tracks the asymmetry of diffuse scattering caused by the so-called size effect, the displacive distortions of the structure towards or away from the $Co(CN)_6$ vacancies. Three regions can be distinguished: region I corresponds to the thermodynamically metastable phase of the flash frozen sample; above 210 K, region II corresponds to the thermodynamic equilibrium phase with average crystal symmetry; region III is found below 200 K in the slowly cooled sample and its appearance is characterised by the jump in the s_2 value.

The effect described by component 2 is more subtle. It mostly contributes to the emergence of *asymmetry* of the diffuse scattering signals with respect to integer reciprocal space indices. Such variations are caused by the so-called size effect: the displacive distortion of the structure towards or away from the $Co(CN)_6$ vacancies (Weber & Simonov, 2012). Note though that components 1 and 2 share some features, possibly due to the orthogonality constraint which is embedded in the SVD analysis.

Based on the evolution of the scale coefficients s_1 and s_2, we can distinguish three regions. Region I is observed in the flash-frozen sample and spans from 90 K to 200 K. It corresponds to the metastable low-symmetry phase of the crystal. This low-symmetry phase is characterised by diffuse clouds, which disappear linearly with temperature. Above 210 K, region II is characterised by an almost parallel trajectory of s_1 and s_2. Since this region is identical on heating and cooling, it corresponds to the thermodynamically stable phase of the crystal with cubic symmetry. Region III is observed on slow cooling below 200 K and is characterised by a sudden jump in s_2, while s_1 continues the evolution of region II. Note that the transition from region II to region III is hidden, since it does not involve a change in crystal symmetry. We could not detect it in the evolution of the unit-cell parameters either, although a similar transition may have been observed as a glass transition in a related PBA by adiabatic calorimetry (Bhattacharjee *et al.*, 2007) where it was associated with the freezing of water degrees of freedom.

Overall, we find that both the flash-frozen sample and the slowly cooled sample show a transition below 200 K. This transition is within the range of freezing of water confined in the small nanopores (Schreiber *et al.*, 2001; Morishige *et al.*, 2010; Neffati *et al.*, 2020). In the following, we present further evidence from 3D-ΔPDF analysis that water indeed plays an important role in this transition.

3.4. Infrared spectroscopy

We have performed infrared (IR) spectroscopy on Mn[Co] to access directly the vibrational bands of water within the nanopores and trace their evolution with temperature. Fig. 7

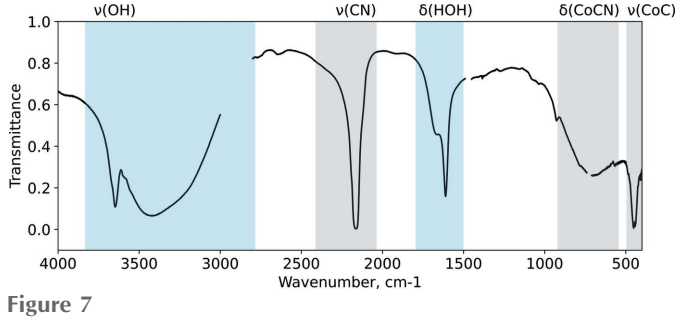

Figure 7
IR spectrum for the Mn[Co] at room temperature. The shaded regions indicate the bands related to water vibrations.

shows the full IR spectrum of Mn[Co] at room temperature in good agreement with the literature (Avila *et al.*, 2008).

The spectrum is characterized by several groups of vibrational bands. The bands observed below 1000 cm^{-1} correspond to ν(CoC) and δ(CoCN) vibrations. The ν(CN) vibration appears at 2100 cm^{-1}. The spectral features related to water vibrations are found at 1600 and 3600 cm^{-1}. The sharp bands at 1610 cm^{-1} and at 3650 cm^{-1} correspond to δ(HOH) bending and ν(OH) stretching and modes of coordinated water. The broad bands, observed below 3500 cm^{-1} and above 1650 cm^{-1}, correspond to vibrations of weakly bonded water (Avila *et al.*, 2008).

We collected IR spectra every 10 K during slow cooling (1 K min^{-1}) cycle. Unfortunately, the cryostat compatible with the IR setup does not allow for flash cooling procedures in comparison to the X-ray diffraction experiments, where the crystal is quickly placed under a cold gas stream using a cryostream system. Therefore, we are limited to the investigation of regions II and III that were identified in §3.3.

While the broad bands around 1650 and 3500 cm^{-1} do not show a discernible change, the ν(OH) stretching and δ(HOH) bending modes, however, show significant changes in spectra. These changes occur as a gradual process across the entire temperature region and show no visible discontinuity near 200 K. In Fig. 8, we trace changes in the IR spectra in 10 K temperature steps (see also Fig. S1 in supporting information for the evolution of spectra in the full measured range).

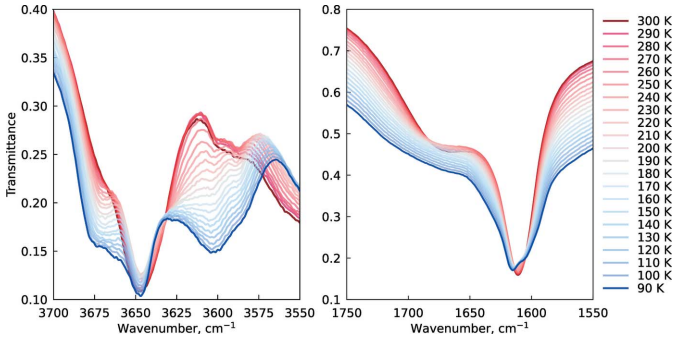

Figure 8
IR spectra for the Mn[Co] in a temperature range from 90 K to RT with ν(OH) stretching bands on the left and δ(HOH) bending vibrations on the right.

The fact that IR data is essentially insensitive to the transition from region II to region III might indicate that structural water (which provides the sharpest IR signatures) is not directly involved in the transition. However, given different sample conditions during diffraction and IR experiment (single crystal versus powder, and nitrogen gas cryostream versus vacuum cryostat), we cannot exclude the possibility that in the IR experiment the transition is completely suppressed, for instance, due to different water contents in the sample. For additional insights of water behaviour under cooling, we continue the analysis of diffuse scattering data with 3D-ΔPDF.

3.5. Redistribution of water observed by 3D-ΔPDF analysis

In contrast to IR, the 3D-ΔPDF is most sensitive to the behaviour of zeolitic water, since the corresponding peaks do not overlap with other PDF signals. It can be best observed in the position $uvw = \frac{1}{6}, \frac{1}{6}, \frac{1}{6}$, which contains the ΔPDF peak from Co to the nearest zeolitic oxygen atom. The ΔPDF signal at this position is negative at all temperatures, implying that if a Co atom is present, the water site is likely empty, and vice versa. At room temperature this ΔPDF peak is weak, and centered at x = 0.21 (Fig. 9, and also Fig. S3 in supporting information), indicating that zeolitic water is still relatively free to occupy most of the available space in the void centered at $\frac{1}{4}, \frac{1}{4}, \frac{1}{4}$ [see Fig. 9(*d*)]. At lower temperatures the peak becomes stronger and its center moves to x = 0.17 for the quenched sample at 90 K and to x = 0.19 for the slowly cooled sample, as the zeolitic water becomes strongly bound to the energy minimum position [illustrated in Fig. 9(*e*)].

The rest of the 3D-ΔPDF is relatively complex and its analysis is beyond the scope of this work. Therefore, we restrict to the following two notes: first, on cooling the distribution of vacancies does not change and stays comparable to the findings by Simonov *et al.* (2020). Second, the small variation in diffuse scattering is caused by the relaxation of Mn and Co atoms.

3.6. Metastable low-temperature structure of Mn[Co]

Now let us understand the structure of the flash frozen Mn[Co] sample. As noted above, diffuse scattering clouds, which mark the emergence of the new metastable phase, indicate the breaking of the high-temperature cubic symmetry

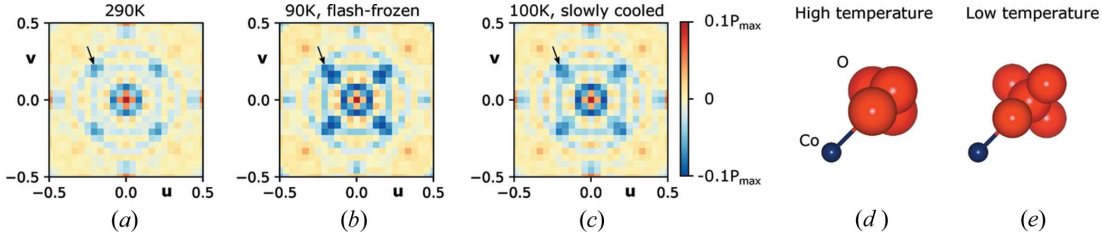

Figure 9
3D-ΔPDF map of Mn[Co] at different temperatures, the section uv0.17 containing the signal from the Co atom to the nearest zeolitic oxygen: (*a*) at room temperature the signal is weak and centred near xxx with x = 0.21 which corresponds to (*d*) a disordered configuration of water; at low temperatures the peak becomes more pronounced and moves to x = 0.17 for a flash-frozen sample, (*b*), and to x = 0.19 for slowly cooled sample, (*c*), which corresponds to a better defined position of zeolitic water, (*e*).

of the material. Unfortunately, all the single crystals of sufficient size for the collection of high-quality diffuse scattering were merohedrally twinned and presented equal fractions of all possible domain states. However, since diffuse clouds from different domains are well separated in reciprocal space, as a first step we have extracted only diffuse scattering that corresponds to the modulation vector $\xi\xi0$.

To achieve this, we have taken intensities of two diffuse clouds around each main Bragg peak at positions $h + \xi, k + \xi, l$ and $h - \xi, k - \xi, l$. The intensities coming from other diffuse scattering as well as the main Bragg peaks were set to zero. Such selection of signals artificially lowers the symmetry of the resulting 3D-ΔPDF map to the Laue group *mmm*. It also simplifies analysis since the effect of one modulation vector is easier to understand. The maximum symmetry with the Laue group 4*mm* can then be recovered by including the full star of modulations containing two vectors $\xi\xi0$ and $\xi\bar{\xi}0$.

The resulting 3D-ΔPDF map is presented in Fig. 10. The *uuw* slice is the easiest to interpret. It consists of the negative-positive-negative or positive-negative-positive peak triplets stretched in the **c** direction [see the inset in Fig. 10(*d*)]. Such triplets are the fingerprints of correlated displacements of atoms along the **c** direction (Weber & Simonov, 2012). The correlation length of the modulation is approximately 25 Å in the *ab* plane, and significantly longer, 50 Å, along the **c** direction.

In Table 1, we present the displacements, which give the best fit to the experimental data. Unfortunately, since in our experiment all Bragg peaks were oversaturated to allow for high-quality diffuse scattering data, we could not estimate the absolute value of the displacement amplitude of the atoms. Thus, we present the amplitudes in relation to the displacements of Mn, which has the highest amplitude. In addition to displacements, in order to reproduce the intensities of satellite reflections, we also had to include the modulation of the atomic displacement parameters U_{xz} and U_{yz} of the cyanide linker. Such modulations are unusual, but are in principle allowed. They do not violate the systematic absence rule, since they do not change the projection of the structure on the *ab* plane, and thus keep the diffuse scattering intensity in the *hk*0 plane exactly equal to zero. Moreover, they are required in this case, since without them model satellites at $h + \xi, k + \xi, l$ and $h - \xi, k - \xi, l$ would always have the same intensities, which contradicts the experiment. The final 3D-ΔPDF calculated from the model is presented in Figs. 10(*b*) and 10(*e*) and provides a qualitative fit to the experimental data.

Table 1
Parameters used to model the low-temperature metastable structure of Mn[Co].

Model parameter	Value
Δz(Mn)	1 a.u.
Δz(Co)	0.27 a.u.
$\Delta z(c)$	0.36 a.u.
Δz(N)	0.9 a.u.
U_{xz}(CN)	$0.35U_{xx}$(CN)

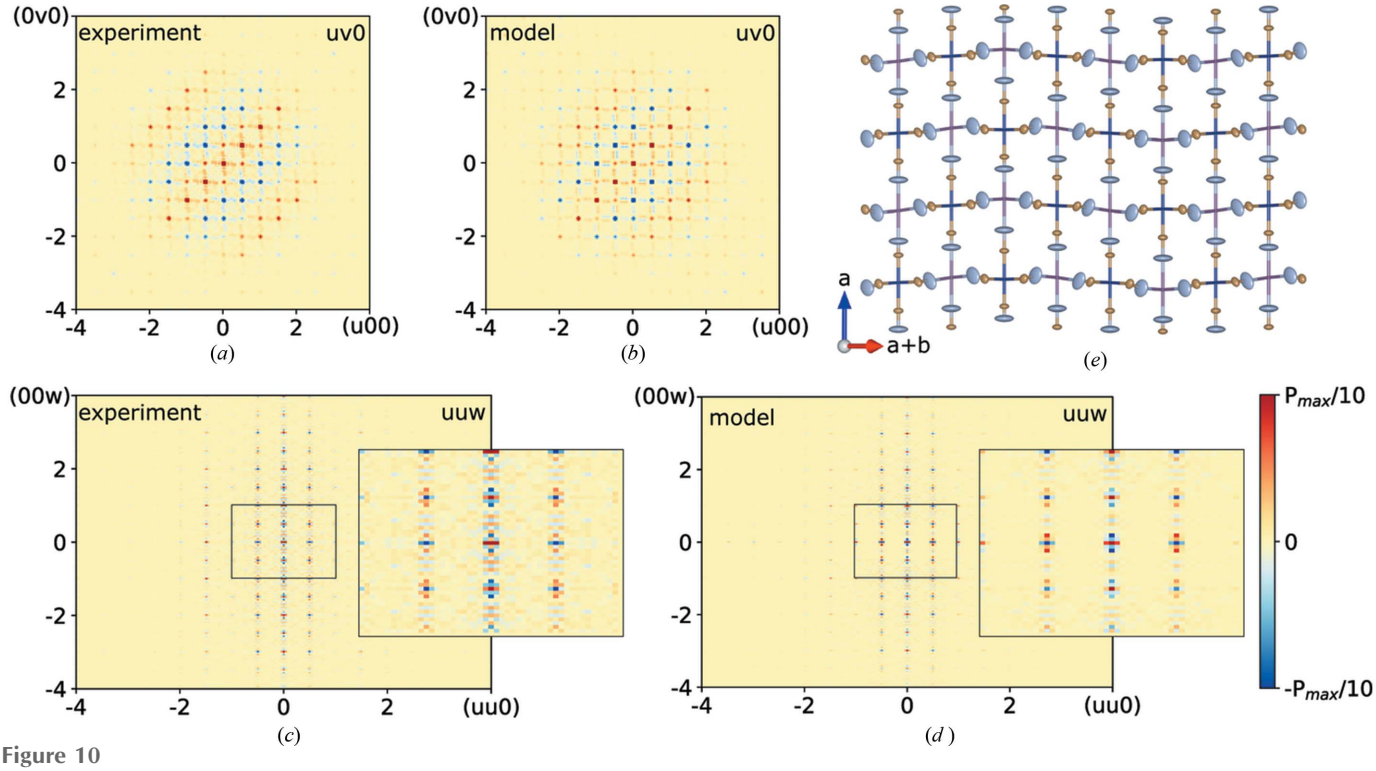

Figure 10
3D-ΔPDF map from only one set of diffuse scattering clouds: *uv*0 plane of (*a*) experimental and (*b*) modelled 3D-ΔPDF map; *uuw* plane of (*c*) experimental and (*d*) modelled 3D-ΔPDF map; (*e*) a portion of the model structure, for clarity modulated atomic displacement and atomic displacement parameters are exaggerated.

The question regarding the symmetry of the low-temperature phase is not trivial, due to the fact that satellites are diffuse, and the structure is not globally, but only locally modulated. However, the highest possible symmetry of the local structure, which is compatible with observed diffraction data, contains two modulation vectors $\xi\xi0$ and $\xi\bar{\xi}0$, and is described by the 3+2-dimensional superspace group $I4/mmm(\alpha00)00s(0\alpha0)00s$ (Stokes *et al.*, 2011).

4. Conclusions

In this paper, we report a novel metastable phase in a flash-frozen Mn[Co] Prussian blue analogue below 200 K. The phase is characterised by the appearance of diffuse scattering clouds and the reduction of symmetry to the tetragonal crystal system. The structure is explained as a disordered structure with incommensurate translational modulation. It is likely that the transition is driven by the freezing of water inside the nanopores created by the $Co(CN)_6$ vacancies which is corroborated by the results of 3D-ΔPDF analysis. Similar diffuse scattering has been previously observed in Cd[Co], Mn[Mn] and Mn[Fe] members of the family, and is most likely a common feature of the disordered cubic Prussian blue analogues.

Fast cooling is essential to observe this phase transition, as on slow cooling below 200 K a different pattern of structural distortions is obtained. This observation highlights the importance of the temperature history for the structure of Prussian blue analogues, and it would be interesting to investigate the influence of the observed phase transition on magnetic properties and the spin crossover which are present in related Prussian blue compounds.

Acknowledgements

AS would like to thank Hans-Beat Bürgi for introducing him to the Prussian blue analogues. AS and YK are grateful to Dmitry Chernyshov and the Swiss Norwegian Beamline at European Synchrotron Radiation Facility (award MA4593), and Lucy Saunders and the I19 at Diamond Light Source (award MT20876) for providing facility for single crystal diffraction experiments. AS and YK would also like to thank Xavier Guichard and Amber Thompson for the help with experiments, and Gregor Kisters for help with the structure modelling.

Funding information

Funding for this research was provided by: Schweizerischer Nationalfonds zur Förderung der Wissenschaftlichen Forschung (grant No. PZ00P2 180035 to Arkadiy Simonov and Yevheniia Kholina, grant No. PZ00P2-179691 to Janine Dössegger) and the Ministère de l'Enseignement Supérieur et de la Recherche and Le Mans University (Mads Weber).

References

Avila, M., Reguera, L., Rodríguez-Hernández, J., Balmaseda, J. & Reguera, E. (2008). *J. Solid State Chem.* **181**, 2899–2907.

Bhattacharjee, A., Saha, S., Koner, S. & Miyazaki, Y. (2007). *J. Magn. Magn. Mater.* **312**, 435–442.

Boström, H. L., Cairns, A. B., Liu, L., Lazor, P. & Collings, I. E. (2020). *Dalton Trans.* **49**, 12940–12944.

Escax, V., Bleuzen, A., Cartier dit Moulin, C., Villain, F., Goujon, A., Varret, F. & Verdaguer, M. (2001). *J. Am. Chem. Soc.* **123**, 12536–12543.

Kabsch, W. (2010). *Acta Cryst.* D**66**, 125–132.

Karyakin, A. A. (2017). *Curr. Opin. Electrochem.* **5**, 92–98.

Kaye, S. S. & Long, J. R. (2005). *J. Am. Chem. Soc.* **127**, 6506–6507.

Kong, Q., Qin, R., Li, D., Zhao, H., Ren, Y., Long, L. & Zheng, L. (2019). *RSC Adv.* **9**, 41832–41836.

Morishige, K., Yasunaga, H. & Matsutani, Y. (2010). *J. Phys. Chem. C*, **114**, 4028–4035.

Neder, R. B. & Proffen, T. (2008). *Diffuse Scattering and Defect Structure Simulations: a cook book using the program DISCUS*, Vol. 11. Oxford University Press.

Neffati, R., Judeinstein, P. & Rault, J. (2020). *J. Phys. Condens. Matter*, **32**, 465101.

Ohkoshi, S.-i., Sato, O., Iyoda, T., Fujishima, A. & Hashimoto, K. (1997). *Inorg. Chem.* **36**, 268–269.

Papanikolaou, D., Margadonna, S., Kosaka, W., Ohkoshi, S.-i., Brunelli, M. & Prassides, K. (2006). *J. Am. Chem. Soc.* **128**, 8358–8363.

Peeters, A., Valvekens, P., Ameloot, R., Sankar, G., Kirschhock, C. E. & De Vos, D. E. (2013). *ACS Catalysis*, **3**, 597–607.

Schreiber, A., Ketelsen, I. & Findenegg, G. H. (2001). *Phys. Chem. Chem. Phys.* **3**, 1185–1195.

Simonov, A. (2019). *Meerkat*: a program for reciprocal space reconstruction. https://github.com/aglie/meerkat.

Simonov, A., De Baerdemaeker, T., Boström, H. L., Gómez, M. L. R., Gray, H. J., Chernyshov, D., Bosak, A., Bürgi, H.-B. & Goodwin, A. L. (2020). *Nature*, **578**, 256–260.

Stokes, H. T., Campbell, B. J. & van Smaalen, S. (2011). *Acta Cryst.*, A**67**, 45–55.

Weber, T. & Simonov, A. (2012). *Z. Kristallogr.* **227**, 238–247.

Wessells, C. D., Huggins, R. A. & Cui, Y. (2011). *Nat. Commun.* **2**, 1–5.